3
Empirical Mode Decomposition Based Algorithm

In this chapter, the threshold based algorithm using half cycle post-fault data is explained. Empirical Mode Decomposition is utilized to extract features from first level residue. Fault and islanding detection, fault classification and fault location in a distribution system are achieved.

3.1 EMPIRICAL MODE DECOMPOSITION

It is a signal processing technique used for analysis of non linear and non stationary information. Using EMD, a time varying signal is decomposed into various oscillating modes known as Intrinsic Mode Functions (IMFs) and a monotonic component known as residue. The number of IMFs formed using EMD depends on the disturbance in the signal [Dalei and Mohanty, 2016]. The signal decomposition is shown in Fig. 3.1, depicting the frequency variation with the order of the IMFs.

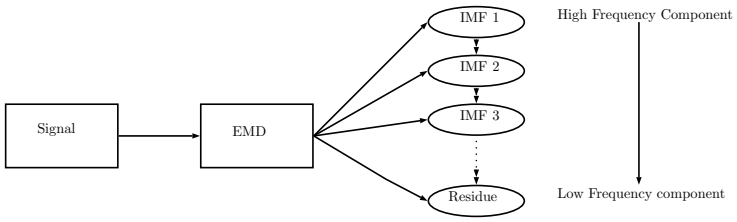

Figure 3.1: Empirical Mode Decomposition.

The decomposed component should satisfy two conditions in order to qualify as an IMF. Firstly, the number of extrema and the number of zero crossing should not be different or at most differ by one. Secondly, the mean value of the envelopes formed by local maxima and local minima should always be zero.

EMD technique comprises of the following steps in decomposition of a given signal $S(t)$ [Nidadavolu *et al.*, 2009]

1. Identification of all the localized maxima (L_p) and localized minima (l_q) of the signal $S(t)$, where, $p, q = (1, 2, ...)$

2. Interpolation of the upper envelope $E_{up}(t)$ and lower envelope $E_{low}(t)$ through cubic spline functions.

3. Computation of the mean value of the upper and lower envelopes of the signal, $M_{11}(t)$ as

$$M_{11}(t) = \frac{E_{up}(t) + E_{low}(t)}{2} \tag{3.1}$$

4. Calculation of the first difference between the signal $S(t)$ and the mean $M_{11}(t)$ as

$$D_{11}(t) = S(t) - M_{11}(t) \tag{3.2}$$

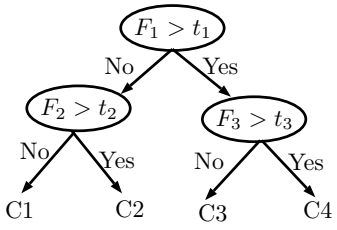

Figure 3.2: A simple decision tree.

5. Verification of $D_{11}(t)$ with IMF properties to designate it as IMF_1

6. Repetition of steps 1-5 by considering the output of step 4 as the original signal. If IMF conditions are met after n iterations, then the output of step 4, $D_{1n}(t)$, would be the first IMF.

$$IMF_1(t) = D_{1n}(t) \tag{3.3}$$

where, $D_{1n}(t)$ is obtained as the difference between the signal at $(n-1)^{th}$ iteration and the mean of the envelopes after the nth iteration,

$$D_{1n}(t) = D_{1(n-1)}(t) - M_{1n}(t) \tag{3.4}$$

7. Computation of level-1 residue by subtracting $IMF_1(t)$ from the signal $S(t)$ considered,

$$R_1(t) = S(t) - IMF_1(t) \tag{3.5}$$

The above mentioned process is repeated using the residue $R_1(t)$ as the original signal. If k iterations of steps 1-7 are executed then $IMF_1(t)$ to $IMF_k(t)$ are extracted along with a residue $R_k(t)$. The EMD process is repeated until $R_k(t)$ becomes a monotonic function from which no new IMF can be extracted. Eventually, the signal $S(t)$ can be reconstructed as

$$S(t) = \sum_{p=1}^{k} IMF_p(t) + R_k(t) \tag{3.6}$$

where, $IMF_p(t)$ is the intrinsic mode function of level$-p$ while $R_k(t)$ is the final residue after k iterations.

3.2 DECISION TREE CLASSIFICATION AND REGRESSION

DT can be applied for classification as well as regression problems. Classification trees predict classes, whereas regression trees predict exact values from a trained set of variables. A binary tree is formed beginning with a decision made at the root node using feature vectors. This binary branching continues with decisions at each node and culminates at the leaf node containing the predicted class or value. For instance, a simple tree is illustrated in Fig. 3.2, where the input feature vectors $F1, F2, F3$ are utilized to predict classes $C1, C2, C3, C4$ by comparing with thresholds $t1, t2, t3$ at each node.

The DT based methods involve a criterion for predicting accuracy, selecting splits or partitions, a stopping condition for splitting and an optimal selection of a tree. The criterion

for the accurate prediction can be done using one of the parameters like re-substitution error, cross-validation error or test sample error. The re-substitution error ($E(c)$) is computed when all the data is used for constructing the tree. It is nothing but a mean squared error between the predicted and actual values and is given as

$$E(c) = \frac{1}{T}\sum_{ts=1}^{T}(v_{ts} - p(u_{ts}))^2 \tag{3.7}$$

where, (u_{ts}, v_{ts}) are the training samples, $ts = 1, 2..., T$. The cross-validation error is computed when the data is divided into subgroups, usually 10, of equal sizes. Initially, the subgroups 1-9 are used for constructing a tree and 10th subgroup is utilized for testing purposes. Next 1-10 subgroups excluding 2nd subgroup are utilized for tree formation and 2nd subgroup samples are utilized for testing. This process continues and the tree with the least error is selected. The cross-validation error for k^{th} subgroup is as follows:

$$E_{cv}(c) = \frac{1}{T_k}\sum_{k}\sum_{(u_{ts},v_{ts})\in X_k}(v_{ts} - p^{(k)}(u_{ts}))^2 \tag{3.8}$$

The test sample error is similar to that of cross-validation error but is computed using an independent test set of equal size as that of the training sample set. The purpose of EMD is to reduce the effect of noise by considering residue based features. The DT model can perform better when outliers due to noisy transients are removed from the healthy phases, thus minimizing the cross validation error and test sample error. The selection of splits is made based on either impurity or node error. A node is pure if it contains only one class. There are various measures for finding the node impurity like Gini Diversity Index (GDI), entropy index, twoing for classification trees. In this work, GDI is employed, and for a node n it is given as

$$1 - \sum_{k} p^2(k) \tag{3.9}$$

where, the summation is for all the classes k at the node, $p(k)$ is the proportion of class k observations at node n.

In the case of regression trees, splits are chosen using the least squared deviation to minimize the sum of squared error between the predicted value and the mean in each node [Moisen, 2008], given by

$$\frac{1}{T_w(n)}\sum_{i\in n} w_{ts} f_{ts}(v_{ts} - \overline{v}(n))^2 \tag{3.10}$$

where, $T_w(n)$ = Weighted number of cases in node n.
w_{ts} = Value of the weighting variable for training case ts.
v_{ts} =Value of the response variable.
$\overline{v}$ = Weighted mean for node n.
f_{ts} = Value of the frequency variable.
The stopping criterion for splitting is determined by the minimum number of nodes. The optimization of the tree is done by pruning method such that the minimum leaf size is obtained with the least error.

3.3 TEST SYSTEM CONSIDERED

The proposed algorithm is tested on two modified IEEE distribution systems consisting of 13 and 34 buses. All the data pertaining to transformers, feeders and loads are obtained from [Kersting, 1991]. Constant impedance load of Δ-Z is used except for Y-Z type at bus 634 for IEEE

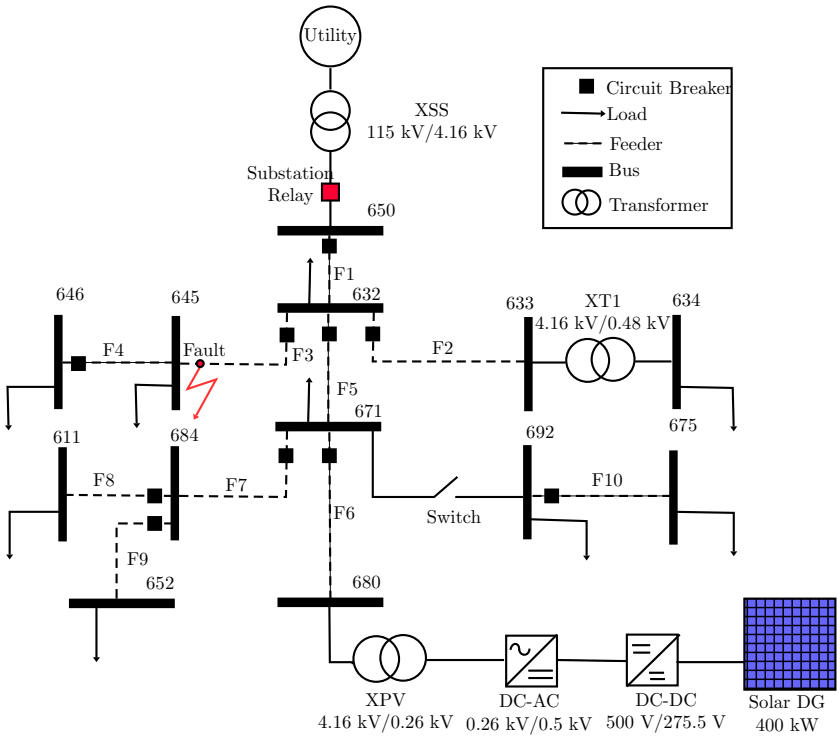

Figure 3.3: IEEE 13 Bus Distribution System.

13 bus sytem. 601 and 606 aerial and underground feeder configurations are utilized whose series impedance matrices are calculated as demonstrated by [Paz *et al.*, 2010]. An IEEE 13 bus system is a 5 MVA, 60 Hz system with two voltage levels of 0.48 kV and 4.16 kV, as shown in Fig. 3.3. Three transformers are used in this study. XSS is a 115 kV / 4160 V, Δ / N-Y transformer having neutral (N) to ground impedance of $(0.5+j\ 0.005)\ \Omega$, and it connects the utility to the distribution system. XT1 is a 4160 V / 480 V, Y-G / Y-G transformer at bus 634 that steps down the voltage for low voltage loads. XPV is a 260 V / 4160 V, Y-G / Y-G interconnecting step-up transformer at bus 680, which connects the solar DG with the network.

IEEE 34 bus system is a 2.5 MVA system with two voltage levels of 24.9 kV and 4.16 kV. A modified IEEE 34 bus system with feeder configurations of 301 and 302 are utilized in this work. The loads considered are three phase balanced except at bus 834. Solar DG of capacity 400 kW is interfaced to the distribution system at 4.16 kV through a transformer XPV at bus 890 as shown in Fig. 3.4. The measurement are done at the substation bus 800. Each 100 kW capacity solar PV plant is connected in parallel to achieve the required capacity at 273.5 V. Detailed specifications can be obtained from [Shaik and Mahela, 2018]. Two converters, the DC-DC boost converter and the DC-AC inverter are used in this study. DC-DC converter boosts the SPV array voltage to 500V using incremental conductance-based Maximum Power Point Tracking (MPPT) technique. The inverter converts the DC voltage to a three-phase ac voltage of 260V.

3.4 PROPOSED ALGORITHM

The fundamental frequency of the test systems considered is 60 Hz with a sampling frequency of 1920 Hz. The faults are simulated at all the buses at 0.5 s except bus 650 for IEEE 13 bus system with a fault resistance of 0.5 Ω, 5 Ω and a ground resistance of 2 Ω. The fault currents measured at the substation for an CAG fault at bus 646 occurring at a fault incidence angle of 120^0 without

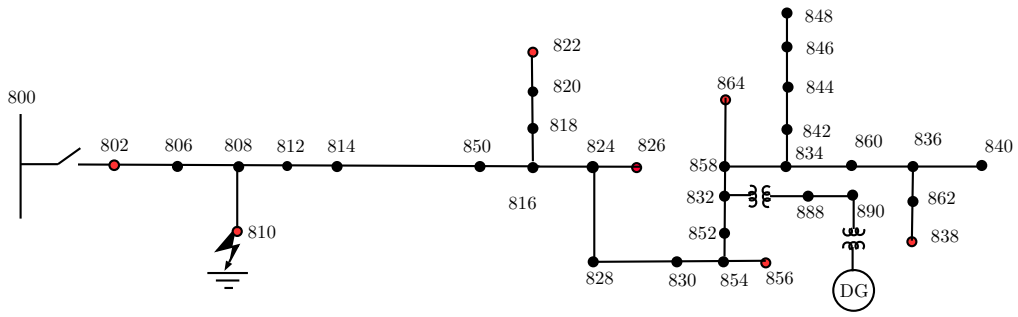

Figure 3.4: IEEE 34 Bus Distribution System.

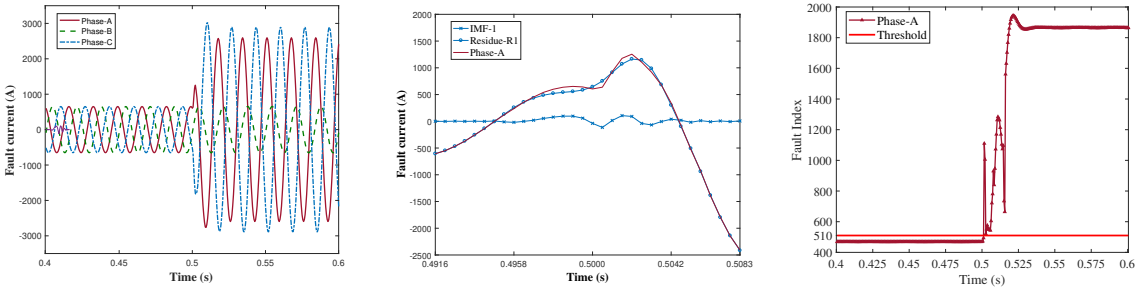

(a) Fault currents

(b) EMD decomposition of Phase-A (16th window)

(c) Fault index of Phase-A

Figure 3.5: CAG fault at bus 646 measured at bus 650.

DG penetration are shown in Fig. 3.5(a). The current samples acquired from a moving window of one cycle duration (32 samples) are decomposed to obtain IMF_1 and residue (R_1) using EMD technique. The higher frequency oscillations are associated with IMF_1 while the R_1 would contain low frequency oscillations. The decomposition of phase-A currents in the 16th window after fault occurrence (half cycle duration after fault) is shown in Fig. 3.5(b).

The standard deviation (SD) of the residue (R_1) is calculated to obtain a fault index value per window for each phase. Thus a fault index vector is obtained for all the phases (A,B and C) as the moving window surpasses the entire current signal. Whenever a fault occurs, the SD of first level residue of faulty phase would have a significant change in comparison to healthy phase, which is utilized for detecting a fault. The variation of fault index for phase-A during CAG fault at bus 646 is shown in Fig. 3.5(c). This fault index is compared with a threshold to detect the occurrence of a fault. A phase index is computed as the maximum value of fault index vector from half cycle post-fault information. The threshold is set after obtaining the faulty phase indices (FPI) and healthy phase indices (HPI) for all the cases considered in the study. A threshold value of 510 is set between the minimum value of FPI and maximum values of HPI and non-faulty transients. The fault type can be classified by the number of phases exceeding the fixed threshold. Thus, if N number of phases exceeds the fixed threshold, then it is called an N-phase fault. If 3 phases exceed the threshold, then it is designated a three-phase fault. We can classify a fault as LL or LLG when N=2, however the involvement of ground could not be ascertained. In order to classify the LL fault from LLG fault, neutral current $I_n = I_A + I_B + I_C$, is utilized to compute a ground fault index FI_G, based on the absolute mean (AM) value of first level residue. If the FI_G is above the fixed threshold of T_G, then it is an LLG fault otherwise a LL fault. After the fault is detected and classified, the fault indices are fed to the machine learning model to exactly locate the fault.

The flow chart of the algorithm proposed is demonstrated in Fig. 3.6.

3.5 RESULTS AND DISCUSSION

3.5.1 Fault Detection And Classification In IEEE 13 Bus System

Effect of fault incidence angle

The proposed algorithm is tested for various fault incidence angles (FIA) of $0^0, 30^0, 60^0, 90^0, 120^0, 150^0, 180^0, 225^0, 270^0, 300^0, 315^0$ and 350^0. It is observed that the proposed algorithm successfully detects the fault for all incidence angles considered. The BG fault at bus 680 occurring at a fault resistance of 5 Ω is shown in Fig. 3.7(a). It can be confirmed that the FPI of faulty phase B is above the threshold for all inception angles. It is also observed that the FPI for 0^0 is the same as 180^0. The fault incidence angles above 180^0 though considered at random, are similar to that of positive half cycle angles $0^0 - 150^0$. Hence, positive half cycle angles are only shown in the rest of the thesis wherever fault incidence angles are considered. ABCG fault simulated at bus 680 is shown in Fig. 3.7(b), it is noted that all the phases are above the threshold. A similar observation can be made in Fig. 3.7(c) for ABG fault where only the healthy phase C is below the threshold.

Change of fault location

The fault transients vary with the location of the fault. Thus 11 types of faults are simulated at every bus except bus 650 as it is used for measurement of the current signals. The maximum value of half cycle post-fault data from the feature vector of faulty phase is defined earlier as faulty phase index (FPI). A Similar term for the healthy phase is defined as the healthy phase index (HPI). In order to set a fault threshold, the minimum value of FPI (FPI_{min}) should always be greater than the maximum value of HPI (HPI_{max}) at every faulty location and for all the cases considered. This necessary condition is satisfied at every location, even in the presence of solar DG, as shown in Table 3.1. It can be observed that the minimum of FPI_{min} for all conditions of fault resistance and noise levels is equal to 519.72, and the maximum of all HPI_{max} is equal to 498.85. It confirms that the proposed algorithm is not affected by the location of the fault. The prescribed threshold value of 510 is chosen closer to the average of the extreme values. Thus all the healthy phase indices would be below the threshold at all locations. The threshold criterion also involves the consideration of the maximum value of FPI during non-faulty transient events as shown in Table 3.3. The threshold in general is chosen as follows:

Threshold = $mean$ {[min (FPI_{min} for all faults considering various variations under study)], [max (max (HPI_{max} for all faults considering various variations under study), max (FPI during all non-faulty transient))]}.

Change of fault type in the presence of noise

The proposed algorithm is tested by contaminating the current signals with random noise of varying standard deviations. The algorithm is immune up to signal to noise ratio (SNR) of 20 dB. The SNR is obtained using equation (3.11)

$$SNR(dB) = 10 * log_{10} \frac{E_{Signal}}{E_{Noise}} \tag{3.11}$$

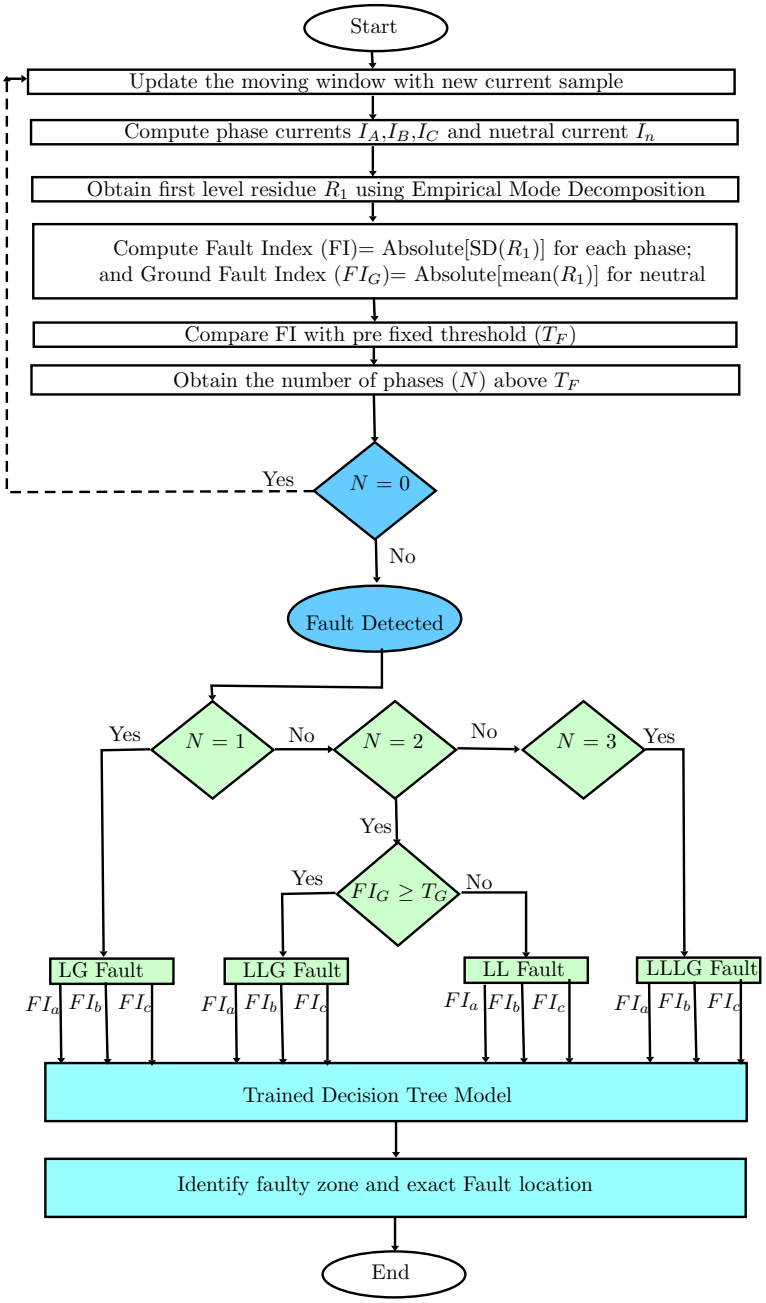

Figure 3.6: Flow chart of the proposed algorithm.

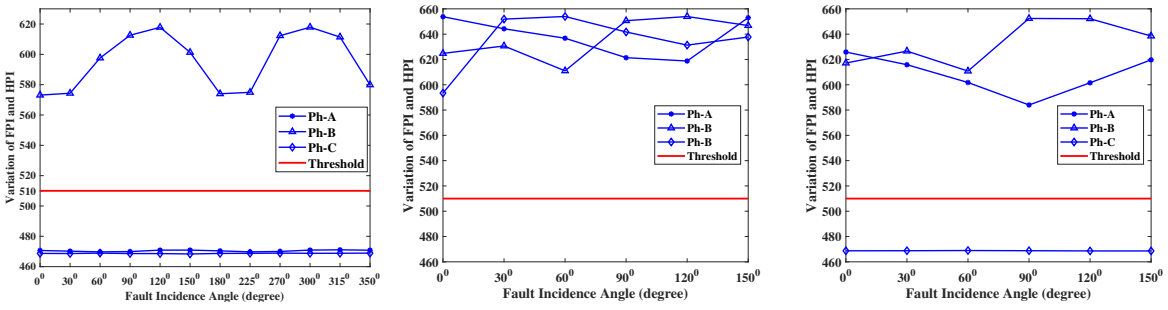

(a) BG fault (b) ABCG fault (c) ABG fault

Figure 3.7: FPI and HPI variation with fault incidence angle at bus 680.

Table 3.1: Fault indices for various fault locations

Fault Location	Without DG								With DG (Solar 400 kW)			
	R=0.5 Ω No Noise		R=0.5 Ω 20 dB Noise		R=5 Ω No Noise		R=5 Ω 20 dB Noise		R=0.5 Ω No Noise		R=0.5 Ω 20 dB Noise	
	FPI_{min}	HPI_{max}	FPI_{min}	HPI_{max}	FPI_{min}	HPI_{max}	FPI_{min}	HPI_{max}	FPI_{min}	HPI_{max}	FPI_{min}	HPI_{max}
611	577.09	471.65	574.69	492.23	556.55	471.24	544.59	489.59	557.68	473.16	562.83	481.05
632	622.30	472.28	582.77	481.14	580.41	471.13	573.71	495.85	549.98	471.08	600.80	472.28
633	617.57	472.29	605.42	484.34	578.91	471.14	574.70	485.11	529.40	469.14	612.74	481.15
634	612.39	472.27	602.07	**498.85**	578.44	471.15	576.57	488.98	571.48	470.80	597.65	480.75
645	616.90	472.17	617.34	488.30	578.79	471.08	575.00	487.02	529.68	469.22	603.95	477.93
646	613.92	472.12	621.18	489.80	577.34	471.06	575.70	485.79	**519.72**	468.96	591.48	486.14
652	576.00	471.60	577.21	488.72	555.62	471.19	545.66	486.28	554.54	470.98	555.19	483.75
671	595.57	472.02	599.14	496.87	566.64	471.38	564.48	478.35	577.49	475.22	597.49	486.03
675	592.51	471.96	589.49	484.19	564.71	471.38	564.96	493.00	573.50	474.13	590.55	486.76
680	588.15	471.87	590.94	488.60	562.77	471.31	570.20	485.84	576.75	479.05	550.55	489.94
684	578.98	471.69	577.38	480.56	557.62	471.26	558.45	483.70	554.26	473.46	560.38	476.68
692	595.55	472.02	601.36	490.70	566.62	471.37	566.10	487.66	577.44	475.19	565.21	486.44

Table 3.2: Fault indices for neutral current.

Case	LL and LLG Fault indices at 20 dB					
	AB_{max}	ABG_{min}	BC_{max}	BCG_{min}	CA_{max}	CAG_{min}
Without DG	0.79	30.10	0.77	29.11	0.78	29.50
With DG	0.78	**8.62**	0.77	8.90	**0.81**	9.46

where, E_{Signal} is the energy of the signal and E_{Noise} is the energy of the random noise. ABCG, BCG and BG faults are considered at bus 671 to prove the immunity to noise of 20 dB SNR. The post-fault data after an ABCG fault at bus 671 with DG and without solar DG confirms a three phase fault as all the phases are above the threshold after 0.5 s as shown in Fig. 3.8(a). Phase-phase-ground fault or LLG fault in phases B and C perfectly has phase A fault index below the threshold with DG and without DG as shown in Fig. 3.8(b). The variation of ground fault index during LL and LLG fault in phases A and C is shown in Fig. 3.8(c). A ground fault threshold value of 5 is set as T_G after analyzing all the phase-phase and phase-phase-ground faults at all locations whose values are enumerated in Table 3.2. The threshold is set between the maximum of AB_{max}, BC_{max} and CA_{max} equal to 0.81 and minimum of ABG_{min}, BCG_{min} and CAG_{min} equal to 8.62. LG fault in phase-B shows that only phase-B is above the threshold, whereas the other phases lie below the threshold as shown in Fig. 3.8(d). Also, it is shown that the fault detection time (FDT), which is the time taken from the occurrence of the fault to the detection of the fault, is less than half cycle even with renewable energy penetration.

Switching Transients

The proposed algorithm must be tested for classifying non-faulty transients also as these can be misinterpreted as faults. Switching off of capacitor banks at buses 611 and 675 with the help of a three phase breaker is carried out at various incidence angles for this purpose. The maximum and minimum values of fault indices are obtained as FPI_{max} and FPI_{min} respectively. These disturbances are simulated in the presence of solar DG also in the presence of noise. The variation of fault index during capacitor switching at bus 675 is shown Fig. 3.9(a). All the phases are below the threshold, indicating no threat. The variation of FPI with FIA is shown in Fig. 3.9(b) where all the phases are below the threshold at 20 dB SNR. Similar non-faulty disturbances like energizing and de-energizing of transformer and feeder at buses 634 and 692 respectively, switching off of load

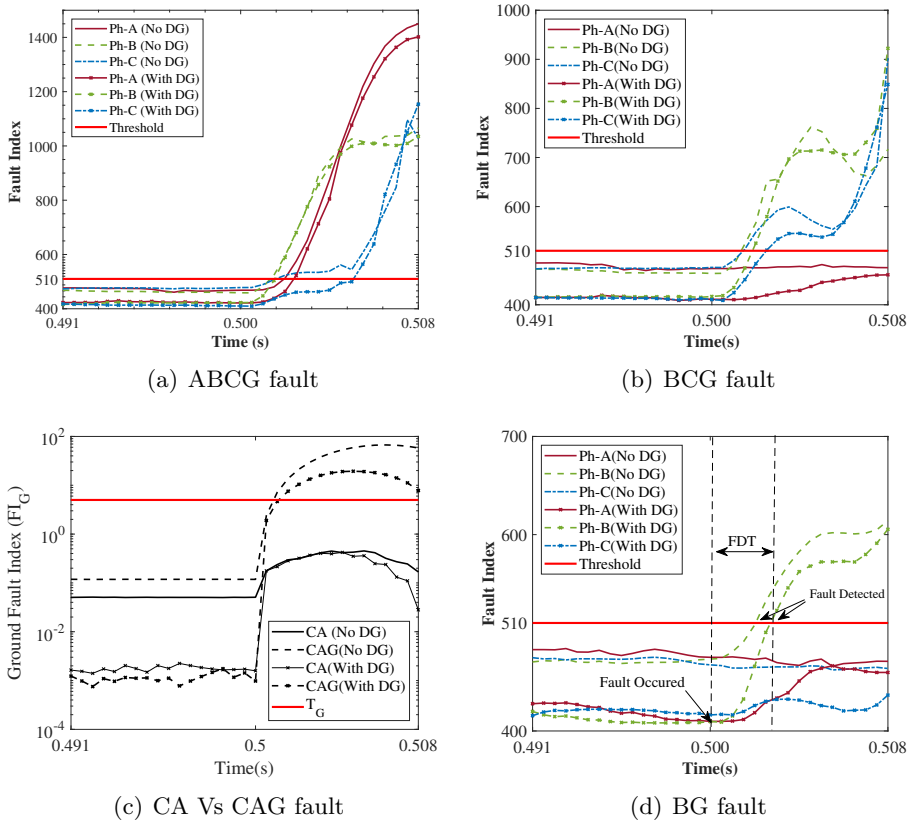

(a) ABCG fault

(b) BCG fault

(c) CA Vs CAG fault

(d) BG fault

Figure 3.8: Fault index variation with type of fault at 20 dB SNR.

Table 3.3: Fault Indices for non-faulty transients.

Disturbance	Without DG-No Noise		Without DG-20 dB SNR		With DG-No Noise		With DG-20 dB SNR	
	FPI_{min}	FPI_{max}	FPI_{min}	FPI_{max}	FPI_{min}	FPI_{max}	FPI_{min}	FPI_{max}
CSOFF at 611	468.88	472.51	473.07	491.34	414.28	417.98	410.07	421.83
CSOFF at 675	469.72	491.53	468.83	**494.58**	415.31	437.72	414.71	448.44
DG Trip	–	–	–	–	414.47	441.64	417.65	454.55
FDE at 692	413.11	436.44	406.62	445.13	357.49	382.46	357.79	386.83
FDOFF at 692	468.62	475.56	466.05	474.26	414.00	421.91	406.52	420.49
Islanding	–	–	–	–	413.55	423.82	411.68	429.05
LDOFF at 652	469.42	469.77	461.83	471.43	414.10	414.41	406.76	416.48
TRE at 634	430.39	444.64	430.22	451.94	375.52	389.78	376.49	396.56
TROFF at 634	469.43	469.93	466.11	479.32	414.10	414.46	418.76	439.67

* CSOFF-Capacitor switch off, TRE-Transformer energizing, TROFF-Transformer de-energizing, LDOFF-Load switch off, FDE-Feeder Energizing, FDOFF-Feeder de-energizing.

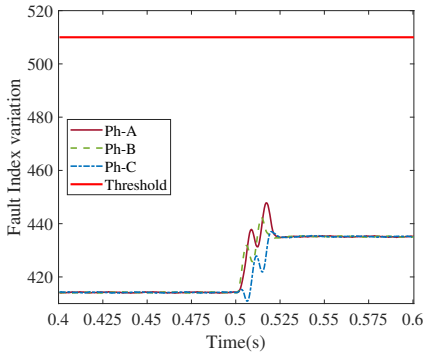

(a) Capacitor switching at 675

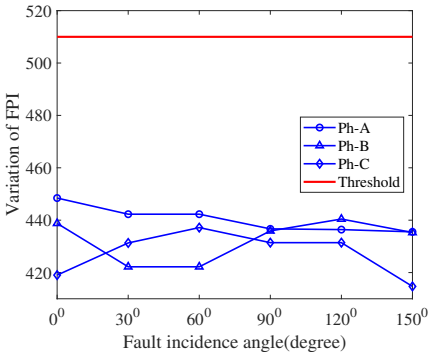

(b) Variation of FPI with FIA

Figure 3.9: Fault index variation with capacitor switching at 20 dB SNR.

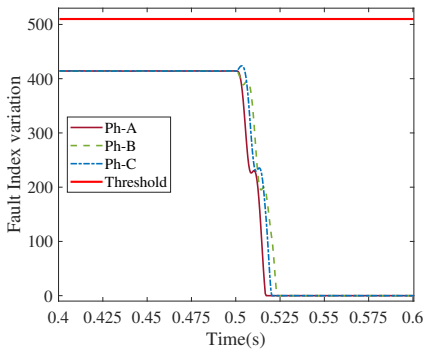

(a) Islanding event

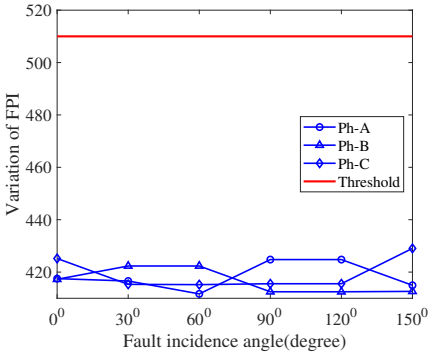

(b) Variation of FPI with FIA

Figure 3.10: Fault index variation with Islanding at 20 dB SNR.

at bus 652 are simulated. The variation of FPI_{max} and FPI_{min} for various fault incidence values are enumerated in Table 3.3. It can be observed that the maximum value of FPI is 494.58, which is less than the threshold of 510. Thus the proposed algorithm is immune to all types of non-faulty transients.

Islanding and DG tripping

The proposed algorithm is also tested for islanding and DG trip cases associated with the penetration of renewable energy sources. The islanding case is simulated by disconnecting the utility from the distribution system using a three phase switch. In the case of islanding, the DG would supply the loads. DG trip case is simulated by disconnecting the DG source at bus 680 using a three phase breaker. The variation of fault index in the case of islanding is shown in Fig. 3.10(a). As the magnitude during this switching event is dependent on incidence angle, the effect of FIA on FPI is shown in Fig. 3.10(b) at 20 dB SNR. All the fault indices are below the threshold, indicating that the algorithm is not affected by islanding. Similar observation can be made for DG trip at bus 680 in Fig. 3.11(a) and Fig. 3.11(b).

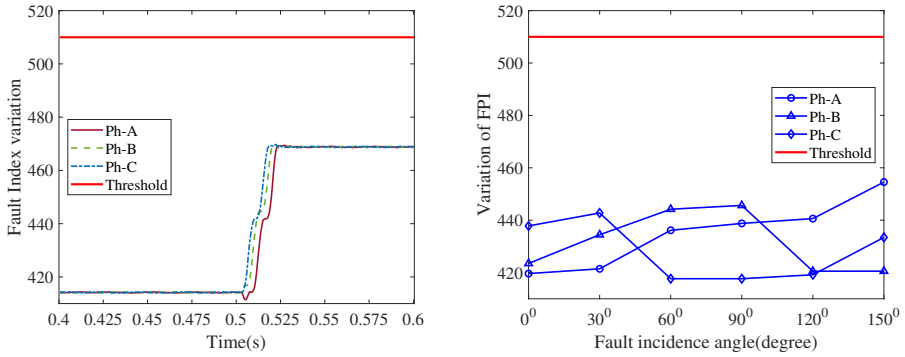

(a) Dgtrip at 680 (b) Variation of FPI with FIA

Figure 3.11: Fault index variation with DG trip at 20 dB SNR.

Table 3.4: Fault indices for various moving windows at 20 dB SNR.

Moving Window	Half cycle post-fault data, R=5 Ω				Half cycle post-fault data, R=0.5 Ω			
	FPI_{min}	HPI_{max}	Margin	T_F Possible	FPI_{min}	HPI_{max}	Margin	T_F Possible
1 cycle	544	495	+49	Yes	574	498	+76	Yes
0.75 cycle	478	481	-3	No	520	485	+35	Yes
0.5 cycle	517	513	+4	Yes	524	514	+10	Yes

Effect of Moving Window

The effect of moving window on the performance of the algorithm is studied, and the FPI and HPI for each case are obtained to observe which moving window size results in more margin. The difference between FPI_{min} and HPI_{max} is the margin. The faulty and healthy phase indices for the feature SD using half cycle post-fault data for fault resistances of 0.5 Ω and 5 Ω at 20 dB noise are presented in Table 3.4. It can be observed that the margin is more for 1 cycle moving window for both the resistance values, thus reducing the chances of misclassification. The threshold is not possible with a 0.75 cycle moving window. The half cycle moving window can be utilized, but it has a less positive margin.

3.5.2 Fault Detection And Classification In IEEE 34 Bus System

The proposed algorithm is tested on an IEEE 34 bus system by considering faults at buses 802, 810, 822, 826, 838, 856, and 864. All the faults are simulated with fault resistance of 5 Ω and ground resistance of 2 Ω without DG and by the penetration of solar DG of 400 kW capacity at bus 890. One cycle moving window is considered to obtain the fault index vector of SD of first level residue. The FPI_{min} and HPI_{max} for all the cases at various noise levels are shown in Table 3.5. The threshold can be set as an average of the minimum of all FPI_{min} equal to 51.53 and maximum of all HPI_{max} equal to 32.20. Thus the proposed algorithm is not affected by the type of the radial distribution system.

Table 3.5: Fault indices for IEEE 34 bus system at 20 dB Noise.

Case	No Noise		40 dB SNR		30 dB SNR		20 dB SNR	
	FPI_{min}	HPI_{max}	FPI_{min}	HPI_{max}	FPI_{min}	HPI_{max}	FPI_{min}	HPI_{max}
Without DG	55.00	31.84	55.10	31.85	54.83	31.88	55.36	**32.20**
With DG	51.56	26.12	**51.53**	26.13	51.60	26.15	51.85	26.10

Table 3.6: Islanding indices for IEEE 13 and 34 bus systems.

	IEEE 13 bus System				**IEEE 34 bus system**			
	No Noise		20 dB SNR		No Noise		20 dB SNR	
Event	FI_1	FI_2	FI_1	FI_2	FI_1	FI_2	FI_1	FI_2
Fault-min	**1456**	165.7	**1487.2**	52.97	**100.20**	15.20	**100.60**	14.07
Island-max	**1252.4**	374.42	**1289.0**	388.71	**63.67**	16.06	**65.23**	16.26
Island-min	1251.4	**269.24**	1223.9	**246.71**	63.64	**10.11**	64.98	**11.00**
Switching-max	1284.8	**143.58**	1328.5	**178.08**	72.58	**6.55**	73.33	**7.53**

3.5.3 Islanding Detection

After the successful fault detection and classification, the islanding is detected by considering the sum of the fault indices of SD and AM for the three phases. Two islanding indices FI_1 and FI_2, are proposed, which are compared with two thresholds TI_1, to distinguish between fault and islanding and TI_2 to discriminate between islanding and switching transient. The fault indices values are enumerated in Table 3.6. For an IEEE 13 bus system, it can be observed that the minimum value of FI_1 during fault is 1456, which is more than the maximum value of FI_1 during islanding in the presence of noise, which is 1289. In order to classify the islanding and switching event, the minimum value of FI_2 during islanding must be greater than the maximum value of FI_2 during switching. It can be ascertained that FI_2 has a minimum islanding index value of 246.71 and a maximum switching index of 178.08, thus discriminating both events. Therefore, TI_1 and TI_2 are set as 1400 and 200, respectively, for IEEE 13 bus system.

For an IEEE 34 bus system, the switching transients considered are CSOFF at buses 844 and 848, FDOFF at bus 816, LDOFF at 802, TROFF at 832, and DG trip at 890. The islanding is simulated by opening the three-phase breaker at the measurement bus of 800. It can be observed that the minimum value FI_1 for fault is 100.60 at 20 dB SNR, which is greater than the maximum value of FI_1 for islanding which is 65.23. Therefore TI_1 is set as 85. In order to discriminate the islanding from switching transient, the minimum value of FI_2 for islanding (11.00) should be greater than the maximum value of FI_2 for switching transient (7.53), which is quite evident. Therefore, TI_2 can be set as 9, which is closer to the average of the extreme values. The proposed algorithm is shown in Fig. 3.12.

3.5.4 Fault Location

The location of the fault is essential for sending the trip signal to the circuit breaker corresponding to the faulty feeder. Decision tree classification (DTC) is utilized for this purpose. The faults are simulated such that a fault on a feeder F1 of an IEEE 13 bus system corresponds to a fault near bus 632. The decision tree employed is optimized for the minimum number of leaves that results in the least re-substitution error and cross validation error. The seven fault locations considered for IEEE 34 bus system are 802, 810, 822, 826, 838, 856 and 864. For an IEEE 13 bus system the faulty zone is located as zone-1 (632, 633, 634, 645 and 646), zone-2 (611, 652 and 684)

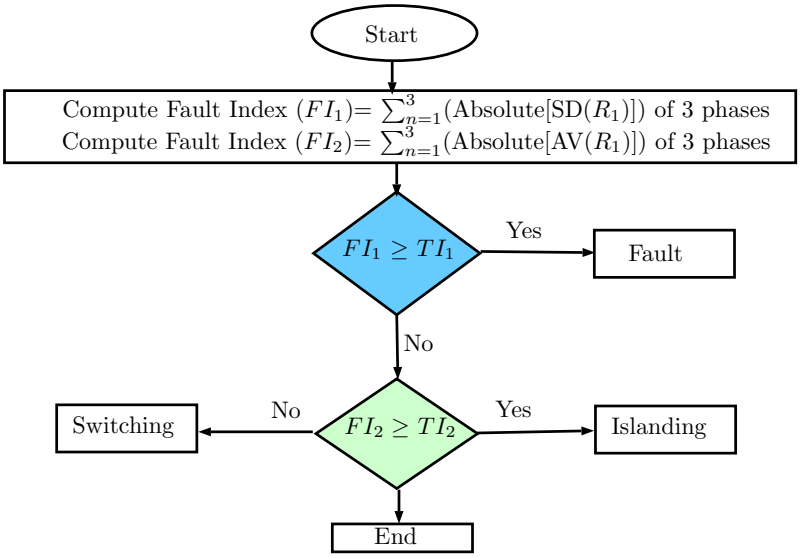

Figure 3.12: Proposed algorithm for islanding.

and zone-3 (671, 675, 692 and 680).

The SD and AM feature vectors are computed for each phase from first level residue itself. The fault indices computed using half cycle post-fault data are fed as input to form decision trees. The case studies involving variations of all fault types, 6 fault incidence angles in steps of 30^0 ($0^0 - 150^0$) and various randomly generated cases at each noise level of 40 dB, 30 dB and 20 dB SNR are obtained at each location. The accuracy is estimated based on the type of the detected fault. Seven modules of DTC are designed based on the fault type namely 3Ph-ABC, 2Ph-AB, 2Ph-BC, 2Ph-CA, 1Ph-AG, 1Ph-BG and 1Ph-CG. The accuracy of the proposed DTC algorithm is given as the ratio of the sum of all correct predictions ($P_{correct}$) to the total number of test cases.

$$Accuracy(\%) = \frac{\sum P_{correct}}{\sum Testcases}.100 \tag{3.12}$$

It is ensured that the total cases at each location are 600 for each noise level. Thus, total cases for each fault module would be, $7 \cdot 600 = 4,200$, at every noise level for an IEEE 34 bus system. The decision tree classification model is designed by training it with 70% of the input data at random and testing with 30% of data unused for training. The fault location accuracy is placed in Table 3.7. It can be observed that the accuracy is high for 3-phase faults but is less for 1-phase faults irrespective of the presence of DG. The overall accuracy or the average accuracy of all the models for IEEE 13 bus system without DG is 83.30% and 94.12% with DG. The overall accuracy for IEEE 34 bus system is 98.22% and 98.46% without DG and with DG respectively.

To compare the proposed work with the existing methods the fault distance is also estimated in the following section. The error in the fault location estimate is determined by Average Error (AE) given by:

$$AE = \frac{1}{N_o}\sum_{n}^{N_o} |D_{Actual}(n) - D_{Estimated}(n)| \tag{3.13}$$

where, N_o is the number of observations, D_{Actual} is the actual fault distance from the substation, and $D_{Estimated}$ is the estimated fault location.

Table 3.7: Fault location accuracy at 20 dB SNR.

Fault	IEEE 13 bus system		IEEE 34 bus system	
	No DG	With DG	No DG	With DG
3Ph-ABC	89.99	98.93	99.76	100
2Ph-AB	85.29	95.32	98.57	98.25
2Ph-BC	91.94	96.06	99.28	98.73
2Ph-CA	83.63	94.62	99.01	98.17
1Ph-AG	66.22	88.88	95.39	97.61
1Ph-BG	82.49	92.63	99.04	98.17
1Ph-CG	83.56	92.40	97.38	98.73
Overall	83.30	94.12	98.22	98.46

Table 3.8: Comparison of fault detection and location times.

Reference	SPT	MLT	FDT	FLT	Buses	Model	SF
[Proposed Algorithm]	EMD	DT	0.5cycle	0.5cycle	13&34	IEEE	1.92 kHz
Deng *et al.* [2015]	DWT	SVM	0.5cycle	0.5cycle	2	Ring	–
Samantaray *et al.* [2008]	ST	PNN	0.5cycle	NC	10	–	1 kHz
Mishra and Rout [2019]	FDST	ELM	1cycle	NC	13	IEEE	3.84 kHz
Mishra *et al.* [2017]	HHT	ELM	1cycle	NC	13	IEEE	3.84 kHz
Shafiullah and Abido [2018]	ST	FFNN	1cycle	NC	13	IEEE	3.84 kHz
Mishra *et al.* [2016a]	DWT	DM	1cycle	NC	6	CERTS	6.66 kHz

3.6 PERFORMANCE COMPARISON

Fault detection and location time

The proposed algorithm is compared with the fault detection time (FDT) and fault location time (FLT) in Table 3.8. The signal processing technique (SPT) and Machine learning technique (MLT) are presented for comparison. It can be observed that fast protection schemes are incomplete without fault location. [Deng *et al.*, 2015] utilized only half cycle post-fault data for feature extraction but it requires measurement at both ends of faulty section and the number of buses of test system are less. However, the proposed technique is implemented on distribution system with more number of buses and also measurement is made at only one location. [Mishra and Rout, 2019] [Mishra *et al.*, 2016a], [Shafiullah and Abido, 2018] and [Mishra *et al.*, 2017] obtained the fault detection time of 1 cycle but fault location is not considered.

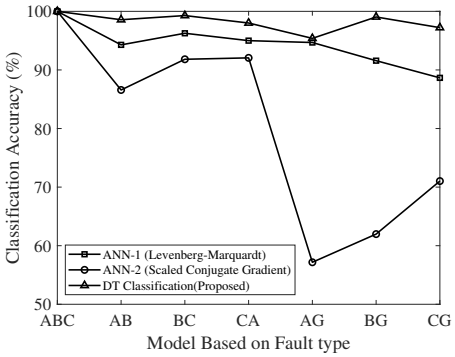

Figure 3.13: Classification accuracy using ANN and DT based algorithms.

Table 3.9: Average error estimated using DT Regression.

Fault Location	IEEE bus system	Distance from substation (m)	Average Error (m) at SNR 20 dB Without DG			Average Error (m) at SNR 20 dB With Solar DG		
			1Ph-AG	1-Ph-BG	1-Ph-CG	1Ph-AG	1-Ph-BG	1-Ph-CG
632	13 bus	609.60	139.80	117.00	120.05	115.10	63.20	80.60
633/634/645	13 bus	762.00	13.40	26.50	25.70	26.40	30.60	32.90
646	13 bus	853.44	103.10	90.90	94.60	90.50	69.10	78.10
802	34 bus	786.38	28.90	3.25e-15	3.06e-15	50.50	2.81e-15	67.30
810	34 bus	12906.45	507.90	127.00	4.65e-4	346.80	9.00e-14	219.30
822	34 bus	51112.27	225.40	76.90	574.00	280.60	85.30	140.60
826	34 bus	35762.54	362.10	7.59e-14	9.57e-14	1038.40	214.60	298.60
838	34 bus	59042.97	238.50	95.60	327.30	377.80	6.50e-14	29.00
856	34 bus	48594.62	401.10	95.60	67.10	275.80	94.30	130.10
864	34 bus	55699.76	183.90	370.60	136.90	210.30	119.60	19.90

Comparison of DT with ANN model

The proposed fault location algorithm is compared with single layer ANN model with 10, 30 and 50 hidden neurons on an IEEE 34 bus system without DG with same features fed to DT. Two ANN models with backpropagation training algorithms based on Levenberg-Marquardt (ANN-1) and conjugate gradient descent (ANN-2) are compared with the proposed algorithm at 20 dB SNR. The classification accuracy for each fault type obtained for 50 hidden neurons with 70% training and 30% testing data is shown in Fig. 3.13. It can be observed that the performance for ABC type fault is 100 % for all models. The accuracy for two phase faults is above 85% for all the models. However, the performance of ANN models decreased for single phase faults in comparison to DT model. The overall accuracy for the proposed algorithm using DT is 98.22%, whereas for ANN-1 model it is 73.08%, 82.04% and 80.18% for hidden neurons of 10, 30 and 50 respectively. For ANN-2 model the overall accuracy obtained is 94.70%, 95.78% and 94.35% for 10, 30 and 50 hidden neurons respectively which is better than ANN-1 but is less than DT.

Comparison of fault distance estimate using DT Regression

The fault location distance is estimated using DT regression for comparing the proposed DT based algorithm with other techniques. The fault locations closer to the measuring bus or less than 1km from the substation are difficult to estimate. The fault locations away from the substation have the least error percentages reported due to variation in the line impedance value with distance. Only frequently occurring single-phase ground fault models are considered here as they are prone to large errors. The results obtained at 20 dB SNR are only discussed as lower noise levels provided better results. For IEEE 13 bus system, the fault locations in zone-1 are regressed using DTR, whereas, for IEEE 34 bus system, fault distance is estimated for seven fault locations considered. For IEEE 13 bus system, the maximum error noticed for closest bus 632 from substation is 139.80m for 1ph-AG fault without DG and 115.10m with DG. The average location error for bus 632 using all single-phase fault models is 125.61m or 20.69% without DG and 86.3m or 14.15% with DG. The higher value of error without DG is due to higher fault resistance considered in comparison to renewable energy case. In the case of IEEE 34 bus system, the average location error for bus 802, which is closest to the substation using all single-phase fault models is 9.66m or 1.22% without DG and 39.26m or 4.99% with DG. As the fault resistance considered is the same with DG and without DG, the renewable energy penetration resulted in higher location error. The fault distance estimates for fault locations closer to substation are presented in Table 3.9. The reported error is less than 91.67% and 52.5% as reported by [Khorramdel *et al.*, 2014] for IEEE 34 bus system and 66.66% and 25% as reported by [Swetapadma and Yadav, 2016] for IEEE 14 bus system. The above comparisons prove that the proposed method is faster and superior to the fault location algorithms proposed for faults close to the substation.

In the proposed algorithm using EMD and DT, for an ABG fault case study on IEEE 13 bus system with 400 kW DG at 20 dB SNR, the features were extracted using EMD within a time of 4.67 ms over a moving window. The machine learning algorithm execution time using DT was approximately 1.985 ms for fault zone location after the feature extraction process. The total elapsed time is obtained on a PC with Intel(R), Xeon(R) CPU E5-2618L v3 @ 2.30 GHz, with 8 GB RAM.

3.7 CONCLUSION

An Empirical Mode Decomposition based protection algorithm is illustrated for a distribution network in this chapter. Three-phase currents obtained at substation are decomposed to obtain first level residue whose standard deviation value, termed as fault index, is compared with a predefined threshold to detect and classify various faults on an IEEE 13 bus and 34 bus systems within half cycle. The case studies which involve changes in fault location, fault incidence angle establishes the robustness of the proposed algorithm with DG penetration. Non-faulty transients such as islanding, tripping of DG, load switching, capacitor switching, and transformer energizing and de-energizing are successfully discriminated from faulty transients demonstrating the selectivity of the proposed algorithm. The unbalanced faults in a grounded distribution network inject transients in healthy phases through neutral. This leads to IMF components in healthy phases also. Hence, the proposed algorithm has preferred to use residue which is free from transients instead of the IMF for the detection of faults to avoid the probability of misclassification. An algorithm to discriminate the islanding and switching transients events is also proposed using the sum of the fault indices of SD and AM computed for three phases. Also, the features based on residue are successfully utilized for fault location in the distribution system using decision tree. The average error in the fault distance estimate for faults closest to the substation is less than existing techniques up to 20 dB SNR. Thus the proposed algorithm can be efficiently utilized for complete fault diagnosis in a distribution network.